JGR Oceans

RESEARCH ARTICLE
10.1029/2019JC015355

Southern Ocean Phytoplankton Blooms Observed by Biogeochemical Floats

Takaya Uchida[1], **Dhruv Balwada**[2], **Ryan Abernathey**[1,3], **Channing J. Prend**[4], **Emmanuel Boss**[5], **and Sarah T. Gille**[4]

[1]Department of Earth and Environmental Sciences, Columbia University, New York, NY, USA, [2]Center for Atmosphere Ocean Science, Courant Institute of Mathematical Sciences, New York University, New York, NY, USA, [3]Division of Ocean and Climate Physics, Lamont-Doherty Earth Observatory, Palisades, NY, USA, [4]Scripps Institution of Oceanography, University of California, San Diego, La Jolla, CA, USA, [5]School of Marine Sciences, University of Maine, Orono, ME, USA

Key Points:
- In situ estimates of phytoplankton biomass and its seasonal cycle are derived based on optical backscatter from biogeochemical Argo floats
- Depth-integrated biomass peaks after mixed layers start shoaling, but accumulation rates turn positive, while mixed layers are deepening
- Biomass is low in Ekman downwelling regions and high in the Antarctic Circumpolar Current and seasonal sea ice zone

Supporting Information:
- Supporting Information S1

Correspondence to:
T. Uchida,
takaya@ldeo.columbia.edu

Citation:
Uchida, T., Balwada, D., Abernathey, R., Prend, C. J., Boss, E., & Gille, S. T. (2019). Southern Ocean phytoplankton blooms observed by biogeochemical floats. *Journal of Geophysical Research: Oceans*, *124*. https://doi.org/10.1029/2019JC015355

Received 10 JUN 2019
Accepted 28 SEP 2019
Accepted article online 17 OCT 2019

Abstract The spring bloom in the Southern Ocean is the rapid-growth phase of the seasonal cycle in phytoplankton. Many previous studies have characterized the spring bloom using chlorophyll estimates from satellite ocean color observations. Assumptions regarding the chlorophyll-to-carbon ratio within phytoplankton and vertical structure of biogeochemical variables lead to uncertainty in satellite-based estimates of phytoplankton carbon biomass. Here, we revisit the characterizations of the bloom using optical backscatter from biogeochemical floats deployed by the Southern Ocean Carbon and Climate Observations and Modeling and Southern Ocean and Climate Field Studies with Innovative Tools projects. In particular, by providing a three-dimensional view of the seasonal cycle, we are able to identify basin-wide bloom characteristics corresponding to physical features; biomass is low in Ekman downwelling regions north of the Antarctic Circumpolar Current region and high within and south of the Antarctic Circumpolar Current.

Plain Language Summary The advent of satellites has allowed us to observe the ocean surface on unprecedented scale. One of the major biogeochemical findings from these observations was that phytoplankton in the Southern Ocean repeatedly went through a dramatic phase of growth every spring basin wide. Phytoplankton, however, exist not only at the ocean surface but also in the interior, generally in the top 100 m. In our study, we revisit the characterization of this spring growth using autonomous floats that vertically profile biogeochemical properties including phytoplankton concentration, providing three-dimensional estimates of phytoplankton. Our results support the conventional knowledge of there being a robust seasonal cycle in phytoplankton within and south of the Antarctic Circumpolar Current region, an energetic eastward current that wraps around Antarctica.

1. Introduction

Phytoplankton are the primary photosynthesizers that convert energy from the Sun to a form that is available to sustain marine life, and they are critical to the biological carbon pump (Deppeler & Davidson, 2017). The biological carbon pump, which involves the production of organic carbon via photosynthesis and export to depth, is argued to be responsible for maintaining ~90% of the vertical gradient of dissolved inorganic carbon (Sarmiento, 2013) and ~10% of the total carbon flux to the deep ocean (Siegenthaler & Sarmiento, 1993). While there is no evidence for any recent global-scale changes in the biological carbon pump (McKinley et al., 2017), its contribution to carbon sequestration may change in a future warming climate (Hauck et al., 2015; Henson et al., 2019; Laufkötter et al., 2015; Moore et al., 2013). Consequently, phytoplankton and biological activity are important contributors to both natural and anthropogenic carbon sequestration via export production and maintaining the dissolved inorganic carbon gradient (Gruber et al., 2019).

The Southern Ocean, along with the overturning circulation (Marshall & Speer, 2012), plays a central role in global biological production. Macronutrients such as phosphate and nitrate are upwelled in the Southern Ocean along with circumpolar deep water, but these nutrients are not fully consumed due to iron limitation (Field et al., 1998; Martin et al., 1990; Moore et al., 2013; Williams & Follows, 2011) and light limitation (Llort et al., 2019). The underutilized macronutrients are circulated to the rest of the ocean basins where

©2019. American Geophysical Union. All Rights Reserved.

they replenish the nutrient depleted surface waters (Dutkiewicz et al., 2005; Moore et al., 2013; Parekh et al., 2004). While the outcropping of isopycnals in the Southern Ocean makes it a globally important region for physical carbon exchange with the deep ocean (Lévy et al., 2013), the importance of Southern Ocean carbon export via sinking and subduction of organic carbon is less certain—estimates range from 8% to 40% of the global export production (Schlitzer, 2002; Siegel et al., 2014; Stukel & Ducklow, 2017). Therefore, a better understanding of the annual cycles of Southern Ocean phytoplankton, which are at the base of marine food webs, can help in better constraining global biological production and local export production.

Estimates of remotely sensed chlorophyll concentration have been important for gleaning insight into the basin-wide magnitude and temporal variability of these blooms (e.g., Ardyna et al., 2017; Moore & Abbott, 2000; Sallée et al., 2015; Thomalla et al., 2011). These studies have shown that surface chlorophyll concentrations observed under clear-sky conditions in the Antarctic Circumpolar Current (ACC) region tend to peak during December and January, coinciding with the periods when the surface ocean is warming and mixed layers are shoaling. While these studies have greatly enhanced our understanding of Southern Ocean biomass, they are limited as satellites only observe the surface concentrations. Behrenfeld (2010) has shown that only knowing the surface concentrations is not sufficient to understand phytoplankton bloom phenology, as periods with deep mixed layers can have active growth that is not easily captured in the surface concentration signal. To circumvent this issue, some recent studies have calculated phytoplankton biomass in the surface ocean by assuming that phytoplankton are vertically homogeneous in the mixed layer (e.g., Sallée et al., 2015). Carranza et al. (2018) recently showed, however, that the biogeochemistry can restratify fairly quickly on the order of 3–5 days, resulting in vertical gradients of phytoplankton within the mixed layer. Lacour et al. (2017), using data from the North Atlantic, also showed that intermittent density restratification within the mixed layer could lead to transient phytoplankton growth even during winter.

In this study, we assess the seasonal cycle of phytoplankton variability in the Southern Ocean by taking advantage of the new biogeochemical (BGC) Argo floats deployed by the Southern Ocean Carbon and Climate Observations and Modeling (SOCCOM) and Southern Ocean and Climate Field Studies with Innovative Tools (SOCLIM) projects. The main focus of our work is to revisit the characterization of the annual cycles of phytoplankton blooms and to understand the dynamics of these cycles. While this is the first study to use in situ BGC Argo floats to characterize bloom phenologies in the Southern Ocean, BGC Argo floats have already started to provide a wealth of insight into the biogeochemistry at work in the Southern Ocean (e.g., Bushinsky et al., 2017; Briggs et al., 2018; Carranza et al., 2018; Gray et al., 2018; Rembauville et al., 2017). Johnson et al. (2017) reported the annual net community production (ANCP), which approximately balances the annual carbon export production, using the nitrate sensors from the floats. Their study is complementary to our work, as they report on the export of total organic carbon from the surface to interior, while we report on the growth and decay of the phytoplankton themselves. BGC Argo floats and gliders equipped with similar sensors have also been used to investigate bloom dynamics in the North Atlantic (Boss & Behrenfeld, 2010; Erickson & Thompson, 2018; Lacour et al., 2017, 2019; Mignot et al., 2016, 2018) and Southern Ocean (Swart et al., 2015).

By using depth-dependent measurements of phytoplankton, we provide an estimate of bloom timing that is independent of previous studies based on satellite observations of surface chlorophyll concentrations. We also show zonally averaged monthly Hovmöller diagrams of phytoplankton biomass and accumulation rates for basin-wide sectors of the Southern Ocean. These diagrams show that, while the biomass peaks in spring/summer, accumulation generally starts significantly earlier—during winter when mixed layers are still deepening.

2. Theory of Phytoplankton Dynamics

Phytoplankton biomass is usually modeled as a concentration field that evolves according to the advection-diffusion equation, along with sources and sinks driven by cell division and loss by mortality and grazing, respectively. This is written as

$$\frac{\partial P}{\partial t} + \nabla \cdot (\mathbf{v}P) = (\mu - l)P + \nabla \cdot \kappa \nabla P - w_s \frac{\partial P}{\partial z}, \tag{1}$$

where $\mathbf{v}$ is the three-dimensional nondivergent velocity field, $\nabla\cdot$ the three-dimensional divergence, κ the small-scale turbulent diffusivity, w_s the sinking velocity (Williams & Follows, 2011), and $\mu(x, y, z, t)$ the phytoplankton division rate, which is a balance between photosynthesis and respiration and generally depends

on nutrient availability, light, and temperature and $l(x, y, z, t)$ the loss rate due to biological processes: mortality and grazing.

Previous studies have commonly averaged this equation appropriately and imposed assumptions, such that the averaged equation describes the evolution of bulk phytoplankton biomass on seasonal time scales (e.g., Behrenfeld, 2010; Mignot et al., 2016, 2018). The horizontal averaging is formally done spatially over length scales of a few eddies and temporally over a few eddy turnover times (~seasonal time scales), and horizontal flux divergence on the left-hand side is assumed to be small. This results in a one-dimensional model for evolution of phytoplankton concentrations. This assumption is a pragmatic one and is partially supported by the observation that the seasonally evolving BGC patterns show spatial coherence over large areas (Mazloff et al., 2018; Moore & Abbott, 2000). It is also common to consider the evolution of vertically integrated biomass, rather than trying to describe the evolution of the vertical profile. Conventionally, this vertical integration is considered over a region where phytoplankton can reproduce and is referred to as the productive layer. Note that the productive layer can be deeper than the euphotic layer if phytoplankton migrate vertically (Forward, 1976) or if mixing is vigorous enough to ensure that phytoplankton spend sufficient time in the euphotic layer to grow. We show our definition of the productive layer in section 3. The horizontally averaged and vertically integrated bulk phytoplankton biomass equation is

$$\left\langle \frac{\partial P}{\partial t} \right\rangle = \langle \mu P \rangle - \langle lP \rangle + w^*(-H)P(-H) - \kappa_v \left. \frac{\partial P}{\partial z} \right|_{z=-H}, \tag{2}$$

where the brackets indicate the vertical integral over the depth of the productive layer ($\langle \cdot \rangle = \int_{-H}^{0} (\cdot) \, dz$). Note that the variables now represent horizontally and temporally averaged/smoothed variables. Here, w^* is composed of time- and space-averaged vertical velocities, eddy driven mean vertical velocities (Fox-Kemper et al., 2008; Gent & McWilliams, 1990), and sinking of phytoplankton. The vertical diffusivity (κ_v) is a result of turbulence driven by winds, shear, and buoyancy-driven convection that is active in maintaining the mixed layer and also the vertical projection of along isopycnal stirring by submesoscale and mesoscale eddies (Balwada et al., 2018; Redi, 1982). The last two terms in equation (2) are evaluated at the base of the productive layer ($-H$) and act as sinks on the bulk biomass because there are no significant phytoplankton concentrations below the productive layer.

The vertical integral of biomass change on the left-hand side of equation (2) can be formally expanded and normalized as $\frac{1}{\langle P \rangle} \left\langle \frac{\partial P}{\partial t} \right\rangle = \frac{1}{\langle P \rangle} \left[\frac{\partial \langle P \rangle}{\partial t} - P(-H) \frac{\partial H}{\partial t} \right]$, where H again is the depth of the productive layer and not the mixed layer as commonly considered. The first term on the right-hand side represents the change in bulk biomass, and the second term becomes negligible at the base of productive layer, that is, $P(-H) \approx 0$. The above discussion leaves us with an equation for the accumulation rate

$$r_p \approx \frac{1}{\langle P \rangle} \frac{\partial \langle P \rangle}{\partial t} = \mu_p - l_p, \tag{3}$$

as a balance between bulk primary production ($\mu_p = \langle \mu P \rangle / \langle P \rangle$) and bulk losses ($l_p = (\langle lP \rangle + \kappa_v \left. \frac{\partial P}{\partial z} \right|_{z=-H}) / \langle P \rangle$) (Behrenfeld & Boss, 2018). In this study we will estimate the bulk biomass ($\langle P \rangle$) and accumulation rate (r_p) using observations, and the above presentation will help us identify potential mechanisms that may set the observed patterns for these variables.

3. Data and Methods

The SOCCOM floats used in this study were APEX and BGC-Navis (Johnson et al., 2017; Riser et al., 2018), while the SOCLIM floats were PROVBIO-2 and PROVAL (Leymarie et al., 2018). All floats were equipped with CTD and bio-optical sensors, which measured temperature, salinity, pressure, nitrate, dissolved oxygen, chlorophyll fluorescence, and optical backscatter coefficient. Additionally, the SOCLIM floats measured incoming photosynthetically available radiation (PAR). Figure 1 shows a summary of the raw data used in this study, which were collected by 152 (144 SOCCOM and 8 SOCLIM) BGC Argo floats. Data from April 2014 to May 2019 were used, but a significant boost in sampling happened in 2016 (Figure 1a). Most of the sampling is around the ACC region, with less sampling in the gyres to the north and Weddell Sea to the south. There is also minor zonal asymmetry in sampling, with less sampling in the Atlantic sector relative to the Indian and Pacific sectors.

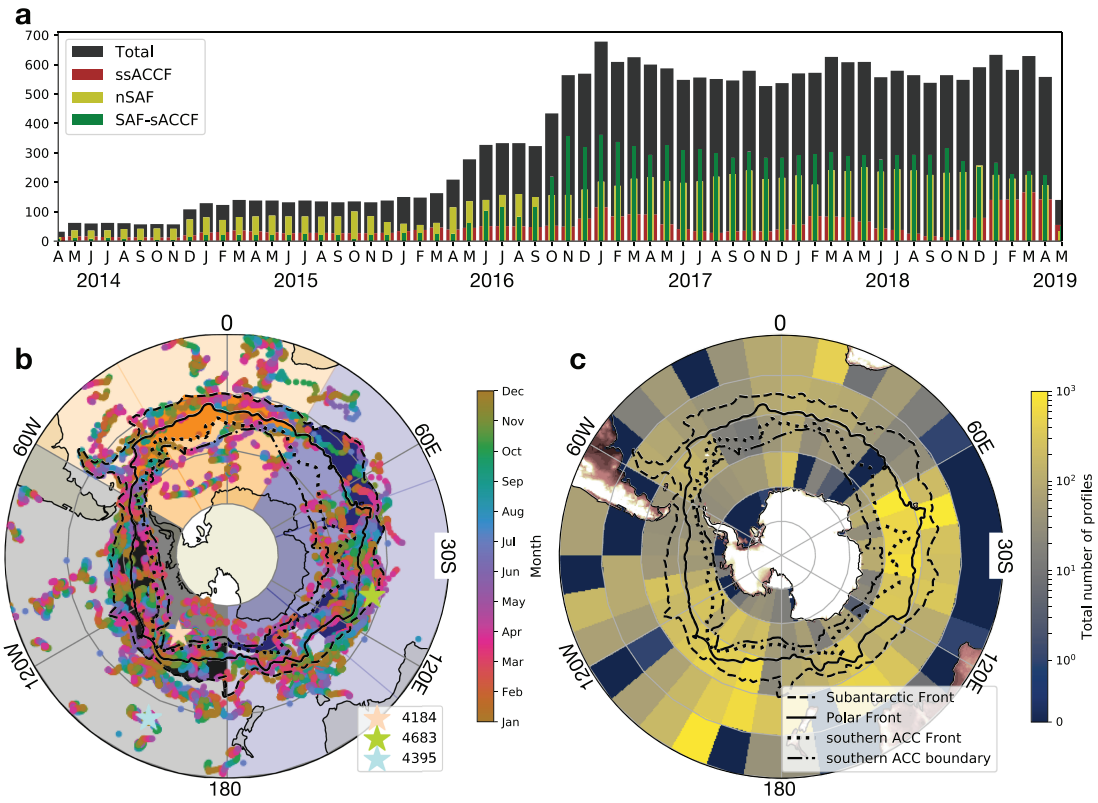

Figure 1. Data availability of the entire SOCCOM and SOCLIM data set. (a) Time series of the number of $\langle C_p \rangle$ data points at any given month of the year with north of the SAF (nSAF) in yellow, between the SAF and the sACCF in green, and south of sACCF (ssACCF) in brown. (b) The geographical location and month of all data points of vertically integrated C_p. The colored shading shows our bioregionalization for each basin (Table 1). The mean position of three representative floats (ID: 5904184, 5904395, and 5904683) are shown as the stars. (c) The cumulative number of profiles over the whole data set aggregated over 10° lat-lon boxes. The SAF, PF, sACCF, and SBdy are shown in black dashed, solid, dotted, and dotted-dash lines, respectively.

We only used the quality-controlled data here; this included data points that had been flagged as good or had been corrected by inspection (as indicated by quality flags–1, 2, 5, and 8; Carval et al., 2014, https://archimer.ifremer.fr/doc/00187/29825/40575.pdf). In situ temperature and salinity measurements were used to calculate the potential density and stratification (N^2) using the Python implementation of the Thermodynamic Equation of Seawater 2010 (McDougall & Barker, 2011, https://teos-10.github.io/GSW-Python/). The mixed-layer depth was defined using the density threshold criterion: the depth at which the density is greater by 0.03 kg m^{-3} relative to 10 dbar (Ardyna et al., 2019; Carranza et al., 2018; de Boyer Montégut et al., 2004). Figures S4–S6 show that this criterion picks up the sharp vertical gradient in stratification.

For the BGC properties of chlorophyll and backscatter, additional processing was required. We used the chlorophyll concentrations that had been corrected for nonphotochemical quenching and the optical backscatter measured at 700 nm. We subtracted out the median of all measurements per float below 600 dbar to account for the potential bias between different measurement technologies and then applied a five-point median filter in the vertical to remove spikes in the profile. Similar methods have been used previously (e.g., Carranza et al., 2018; Erickson & Thompson, 2018; Mignot et al., 2018). The removal of the deep median assumes that nonzero values at depth are generally a result of an instrument bias and background values of backscatter rather than true phytoplankton-related signal. The despiking removes measurement noise or potential signal due to aggregates. In order to correct for the known bias between measurements by Argo floats and shiptrack high-performance liquid chromatography (HPLC), we first doubled the corrected chlorophyll concentrations to account for the global factor of 2 (Roesler et al., 2017) and then adjusted them based on an empirical fit for each data set: $\mathrm{Chl}_{\mathrm{HPLC}} \approx 0.21 \times \mathrm{Chl}_{\mathrm{SOCCOM}}^{0.714}$ (Johnson et al., 2017; Haëntjens et al., 2017) and $\mathrm{Chl}_{\mathrm{HPLC}} \approx \mathrm{Chl}_{\mathrm{SOCLIM}}/3.46$ (Roesler et al., 2017, Table 1 in their paper). Henceforth, we drop the subscript $(\cdot)_{\mathrm{HPLC}}$, i.e., $\mathrm{Chl} = \mathrm{Chl}_{\mathrm{HPLC}}$.

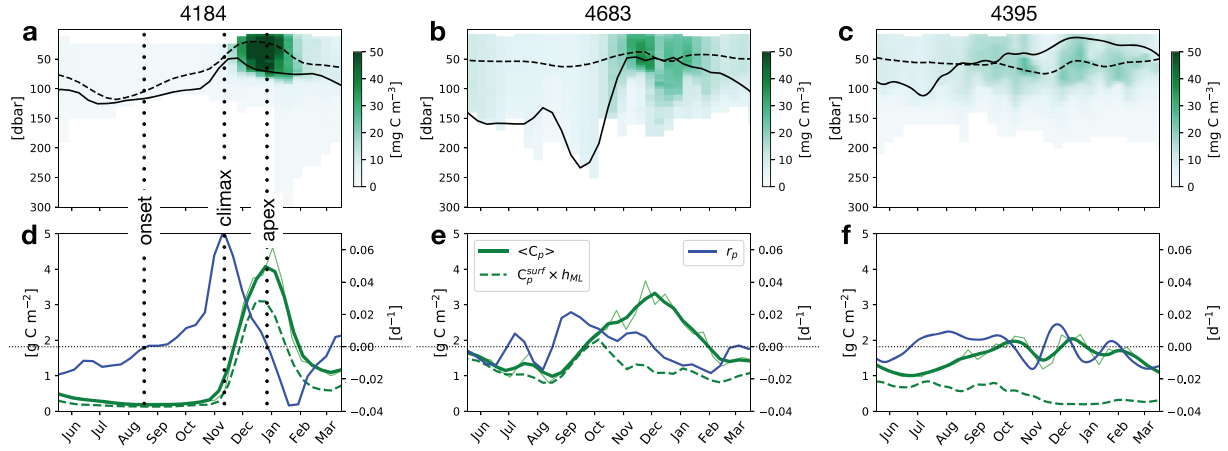

Figure 2. Time series of despiked and interpolated C_p masked out based on the Chl cut off (a–c) plotted against pressure for the floats shown in Figure 1b. The full time series of each float is given in Supporting Information S1. The black solid (dashed) lines show h_{ML} (h_{PAR}). (d–f) Time series of the vertically integrated carbon $\langle C_p \rangle$ in green solid, surface carbon concentration multiplied by h_{ML} in green dashed, and accumulation rates (r_p) in blue solid lines after a 30-day running mean is applied. The thin green lines show $\langle C_p \rangle$ before the running mean.

Phytoplankton carbon biomass was estimated using the backscatter data. This process required first converting the backscatter observations at 700 to 470 nm, using $b_{bp}(470) = b_{bp}(700)\left(\frac{470}{700}\right)^{-0.78}$. The estimated 470 nm backscatter was then converted to phytoplankton carbon biomass (C_p) using the empirical linear relationship from Graff et al. (2015): $C_p = 12,128 b_{bp} + 0.59$. This relationship was obtained by comparing simultaneous measurements of in situ phytoplankton carbon biomass and backscatter, using data from cruises in the North and South Atlantic and the Western Pacific Ocean. The R^2 coefficient of the linear regression was 0.69, and the root-mean-square error in phytoplankton carbon biomass around the empirical relationship was 4.6 mg C m^{-3}. While this empirical relationship is not perfect, it has previously been applied to estimate net primary production globally (Silsbe et al., 2016) and C_p in the Southern Ocean (Haëntjens et al., 2017), and it is consistent with Behrenfeld et al. (2005) in which net primary production was first derived based on b_{bp}.

As different floats had different temporal and vertical sampling frequencies, we interpolated the data for each float onto uniform temporal grids with time steps equal to the minimum temporal sampling rate for each float and a stretched pressure grid from 4 to 1,000 dbar with a resolution of 4 dbar in the upper 100 and 10 dbars below. The interpolation was done in Python using a piecewise cubic Hermite interpolating polynomial (pchip) scheme. In order to avoid including nonphytoplankton particulate organic matter in our calculation, we masked the backscatter data using a mask built under the assumption that phytoplankton biomass would have appreciable levels of associated chlorophyll. A cutoff Chl per float was defined as the 90th percentile of concentrations deeper than 200 dbar, namely, we mask out C_p and Chl below this concentration. The bulk biomass $\langle C_p \rangle$ is then defined by vertically integrating the masked C_p over the whole water column. The depth of 200 dbar was chosen as it was always deeper than the depth where PAR attenuated to 1% of its surface value (h_{PAR}; Text S1). Here h_{PAR} was estimated from the empirical relation provided by Morel et al. (2007, eqn. 10 in their paper, using surface Chl [Chl^{surf}] as the average of top 50 dbar similar to what satellites would observe.). The bulk biomass $\langle C_p \rangle$ was insensitive to this depth scale (200 dbar) and percentile value (90%) chosen for masking out backscatter below the productive layer; our algorithm was able to capture phytoplankton within the mixed layer year round, and the difference in the parameter choice only affected the depth below the mixed layer at which backscatter was masked out (Figures 2 and S4–S6). We show the robustness of our algorithm in Text S2 by changing these parameters.

The floats are advected approximately with the flow at 1,000 m. Thus, changes in the time series of phytoplankton observed by an individual float can potentially be a result of a float crossing through a region of distinct productivity or a patch of distinct productivity at the surface being advected relative to the flow at 1,000 m. However, averaging over large regions and performing a temporal smoothing to extract only the slowly varying seasonal signal, as done in section 4, allows us to capture the broad regional-scale seasonal signals of phytoplankton evolution, which are of interest in this work. This notion is supported by previous

Table 1
Definition of Each Biogeochemical Zone Per Sector We Consider and Approximate Correspondence Between Our Zones With Ardyna et al. (2017)

Basin	Relative to fronts	Ardyna's bioregion
Pacific (60–180°W)	North of SAF	2
	Between SAF and sACCF	4 and 5
	South of sACCF	6 and 7
Atlantic (30–60°W)	North of PF	3
	Between PF and SBdy	4 and 5
	South of SBdy	6 and 7
(30°W to 30°E)	North of SAF	3
	Between SAF and sACCF	4 and 5
	South of SACCF	6 and 7
InTas (30–70°E)	North of SAF	3
	Between SAF and PF	4 and 5
	South of PF	6 and 7
(70–130°E)	North of SAF	3
	Between SAF and sACCF	4 and 5
	South of sACCF	6 and 7
(130–180°E)	North of sACCF	3
	Between sACCF and SBdy	4 and 5
	South of SBdy	6 and 7

Note. Each zone is shown geographically in Figures 1b and 4b.

studies that observed broad regions over which similar seasonal cycles manifest themselves (Ardyna et al., 2017; Thomalla et al., 2011). Additionally, apart from the floats in the ACC, most floats do not traverse very large distances over a year, and so the results are not expected to be contaminated by a single float having seen two dramatically different phytoplankton blooms in a year of sampling.

While considering potential mechanisms that describe the observed patterns, we employ the surface heat flux and surface wind stress from the Biogeochemical Southern Ocean State Estimate reanalysis (Verdy & Mazloff, 2017) and Archiving, Validation and Interpretation of Satellite Oceanographic Data (AVISO)-based map of absolute dynamic topography and surface geostrophic eddy kinetic energy (EKE; https://www.aviso.altimetry.fr). In particular, we define the climatological position of the Subantarctic Front (SAF), the Polar Front, the southern ACC Front (sACCF) and the southern boundary of the ACC (SBdy) along the isolines of map of absolute dynamic topography coinciding with its horizontal gradient maximum (Swart et al., 2010). Details are given in Text S3.

4. Results

4.1. Biomass Cycles From Individual Floats

The Southern Ocean is known to have a wide variety of distinct cycles of biomass growth and decay, as observed by satellites (Ardyna et al., 2017; Sallée et al., 2015). These cycles are generally associated with light availability, circulation, mixed-layer properties, and external iron sources in the region. Here we show three qualitatively different cycles observed by three individual SOCCOM floats, with insight from previous studies that the seasonal sea ice zone (SIZ), ACC, and subtropical zone have distinct bloom phenologies (Arrigo et al., 2008; Sallée et al., 2015). The mean locations of these floats are indicated in Figure 1b as stars. We will use the terminology *onset*, *climax*, and *apex* to characterize the bloom cycle (Behrenfeld, 2010). Each phase is defined using the time series of the vertically integrated biomass ($\langle C_p \rangle$) as (i) *onset*: $\langle C_p \rangle$ minimum ($r_p = 0$), (ii) *climax*: r_p maximum, and (iii) *apex*: $\langle C_p \rangle$ maximum ($r_p = 0$), where r_p was calculated from equation (3) by substituting P with C_p (Behrenfeld & Boss, 2018; Llort et al., 2015; Mignot et al., 2018; Sallée et al., 2015). The vertically integrated biomass time series discussed in this study, examples shown in Figures 2d–2f, have been smoothed using a 30-day running mean. This temporal mean is applied prior to computing the results shown in the remainder of our study. This smoothing minimizes the impact of high-frequency events, such as synoptic storms, which are not well resolved by the 10-day float sampling

of most SOCCOM floats, and therefore highlights variability on seasonal time scales. As the time series presented here might potentially be sensitive to the possibility of floats traversing from one BGC region to another, we purposely chose floats that stayed in the same frontal regions (Table 1 and Figure S3a), which roughly coincide with the bioregions defined by Ardyna et al. (2017), and did not show dramatic changes in water mass properties (Figures S4–S6).

The first float (Float ID: 5904184) is located south of the climatological SBdy in the Ross Sea, which is a region covered by sea ice with limited PAR during austral winter (Figures 2a and S3a). This particular float happened to be under ice from around July to November, as indicated by the missing data in the top 10 dbar for this period when the float's ice detection algorithm did not allow it to surface. During the period of ice coverage, both the phytoplankton biomass concentration C_p and bulk phytoplankton biomass $\langle C_p \rangle$ were negligibly small. The melting of sea ice at the end of November, which allows light to enter the water column and presumably also supplies iron, is coincident with a massive growth in phytoplankton with $r_p \approx 0.07 \quad \text{day}^{-1}$ at its climax (Figure 2d). This also happens at the time when the mixed layer is at its shallowest. Surface biomass concentration C_p^{surf} is consequently tightly coupled with $\langle C_p \rangle$ throughout the bloom cycle. However, this growth is short lived, approximately 1–2 months, and the bloom starts to decay by the end of January.

The second float (Float ID: 5904683) is located downstream of the Kerguelan Plateau and drifts along the Subantactic Front (SAF; Figures 2b and S3a). This is a region of vigorous eddy activity, and the presence of the Kerguelan Islands and hydrothermal vents can act as a source of lithogenic/benthic iron here (Ardyna et al., 2019; Blain et al., 2008; Bowie et al., 2015; Gille et al., 2014; Schallenberg et al., 2018). This float happened to see a short-lived period of growth in July, but the onset to apex is from August till the end of December. Considering that the onset is before the wintertime mixed-layer depth maximum, it is likely that the increase in phytoplankton is due to the reduction of grazing pressure (Behrenfeld, 2010) and/or an increase in PAR (Llort et al., 2015). The climax ($r_p \approx 0.02 \quad \text{day}^{-1}$) is during a period when the mixed layer is deepening, while the maximum in surface concentrations and bulk biomass are seen when the mixed layers are their shallowest (Figure 2e). During the period when the mixed layers are shallow, between December and February, instances of phytoplankton biomass existing below the mixed-layer depth are also observed.

The last float (Float ID: 5904395) considered in this section is located in the quiescent Pacific subtropical zone north of the SAF (Figures 2c and S3a). This is a region where light is plentiful year round, but macronutrients might be limited due to the presence of a strong thermocline (Carranza & Gille, 2015). The deepest observed mixed layers (~100 m) are not significantly different from the expected depth of the euphotic layers. This float experiences slow biomass accumulation ($r_p < 0.01 \quad \text{day}^{-1}$) onsetting in July and extending all the way till February, along with short periods of decay during this period during November and January (Figure 2f). This bloom cycle differs from the two discussed above, as there is no single dominant apex but instead a broad period when bulk biomass fluctuates at values slightly greater than the annual background with the majority of phytoplankton existing below the mixed layer during austral summer (October–February). Carranza and Gille (2015) found evidence that transient mixed layer deepening associated with high-frequency winds can supply nutrients that alleviate the nutrient limitation both in the ACC and subtropical latitudes, driving episodic increases in productivity with stronger signals in the latter zone.

Only the under-ice float observes periods when the bulk biomass becomes negligibly small during onset, while the other two floats observe regions where there is a nonnegligible level of background bulk biomass year round using backscatter as a proxy. It is possible that nonphytoplankton sources can produce nonzero backscatter signal during parts of the year, but our algorithm to account for backscatter only coinciding with chlorophyll reduces this possibility. While backscatter may not be an exact estimator of phytoplankton concentrations and bulk phytoplankton biomass, it presents a faithful pattern of observed seasonal variability, which is the focus of this study.

4.2. Temporal and Spatial Variability in Bloom Phenology

In section 4.1, we showed three examples in which the bloom cycles can be described by the timing of the three phases: onset, climax, and apex. While synoptic variability can complicate the precise timing of each phase, phases are useful to qualitatively distinguish blooms. Here, we present the median and distribution of the different bloom phase timings and strength of the bloom itself to draw basin-wide characterizations. Ardyna et al. (2017) showed that bloom dynamics are organized in distinct bioregions that roughly coincide with the fronts of the ACC. Motivated by this, we divide the Southern Ocean into three sectors: the Pacific (60–180°W), Atlantic (60°W to 30°E), and the Indian and Tasman Sea (InTas; 30–180°E). We then further

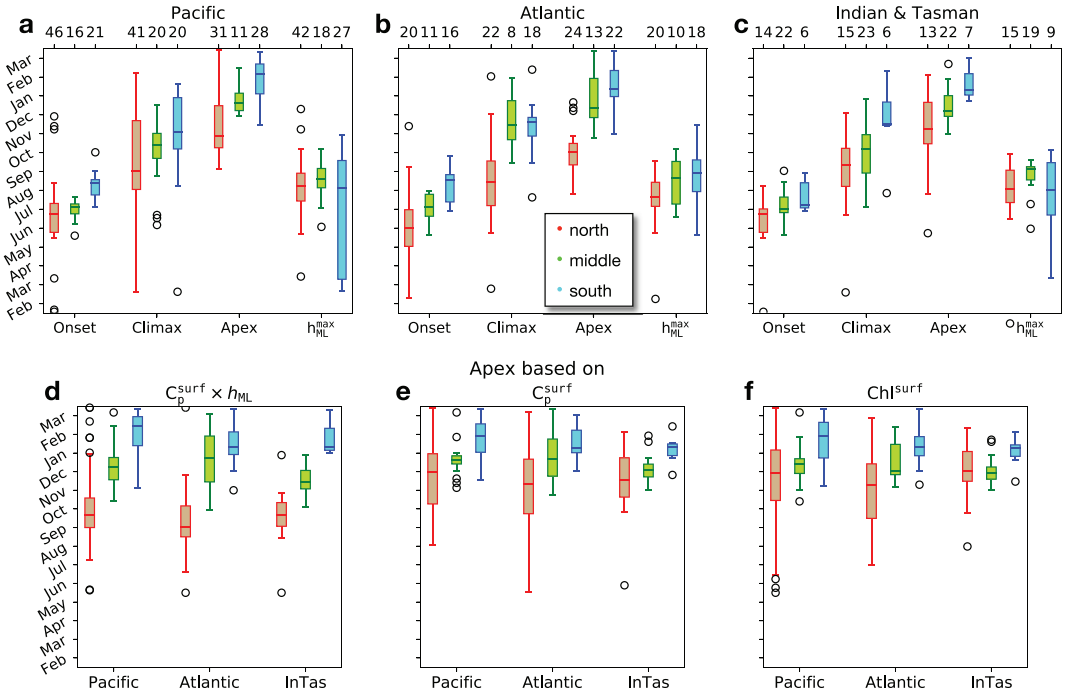

Figure 3. Box plot of the month each spring bloom phase (onset, climax, and apex) and mixed-layer depth maxima takes place for the Pacific (a), Atlantic (b), and InTas (c) sectors defined in Table 1. The northernmost zones are shown in orange, southernmost in blue, and middle in green for each sector. The solid line within the box shows the median, boxes the interquartile range, and whiskers the 95th percentile. The top *x* axes show the number of data points that go into generating the box plots. (d–f) Apex timing detected by the time series of proxy bulk biomass, C_p^{surf} and Chl^{surf}.

separate each sector into north, middle, and south based on the climatological position of the fronts and use these regions to average the float data. The choice of these regions results in similar bioregions to those detected by Ardyna et al. (2017). The approximate correspondence between our zones and Ardyna's bioregion described in Table 1 is shown in Figures 1b and 4b as colored shadings. We do not have sufficient data coverage to define a zone corresponding to Ardyna's Bioregion 1. In order to avoid detecting erroneous minima and maxima in $\langle C_p \rangle$ and r_p due to some time series starting or ending midyear, we require each yearly time series to start before July and end after October when detecting the *onset*, start before August and end after November for *climax*, and start before October and end after December for *apex*. In cases with time series that have multiple local extrema (e.g., Figure 2f), we use the global extremum in defining each phase. The 5-year long data set, starting on 7 April 2014 and ending on 11 May 2019, yielded a total of 228 onset, 222 climax, and 229 apex events (Figure S10).

Figure 3 shows the box plots of the timing of each bloom phase and deepest mixed layer for different zones defined in Table 1. The median onset timing shifts from around June–July in the northernmost zone (red in Figure 3) to July–September in the southernmost zone (blue in Figures 3). Correspondingly the median apex timing shifts from October–December to January–February, which roughly coincides with the transition in the timing of surface chlorophyll maxima from Bioregions 2 to 7 in Ardyna et al. (2017, Figure 2 in their paper). By definition, the climax lies in between the two phases. The large range (3–6 months), in the timing of each phase, is a likely a combined result of spatial and interannual variability. The range of the onset timing is generally smaller than the range of climax or apex timing, suggesting that blooms have a relatively well-defined onset timing. The shift in onset time to later in the year further south, and its narrow range, confirms that the well-defined annual cycle of insolation, influencing the mixed-layer depth and consequently grazing pressure (Boss & Behrenfeld, 2010) and light availability (Llort et al., 2015), is the primary control on initiating the bloom.

The timing of mixed-layer depth maxima relative to the onset date shows that in the northernmost and middle latitude bands, the bloom begins, while the mixed layer is still deepening, while the climax happens after the mixed layer has started to shoal; bloom onset occurs in winter/autumn, and blooms increase in

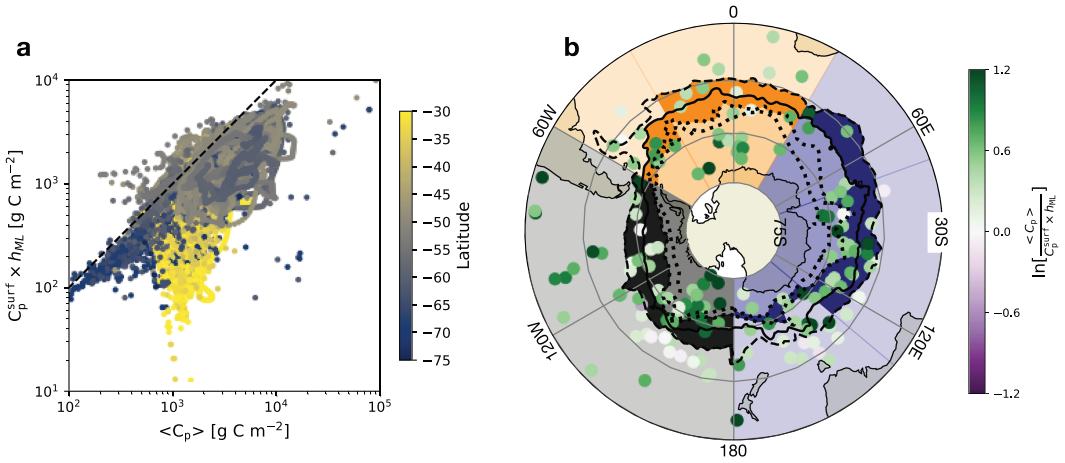

Figure 4. Scatter plot of $C^{surf} \times h_{ML}$ plotted against $\langle C_p \rangle$ (a). The black dashed line indicates the one-to-one ratio. (b) Ratio of $\langle C_p \rangle$ and $C^{surf} \times h_{ML}$ at the apex defined by the global maximum of each variable plotted against geographical location. The Pacific sector is shown in black, Atlantic in orange, and InTas in blue. The middle zones for each sector defined in Table 1 are shown in the darkest shadings and lighter shadings to the north and south, respectively.

production in the spring. The blooms to the south of the sACCF/SBdy, however, most of which are in the SIZ, have a different phenology. Here bloom onset occurs generally during or after the timing of the deepest winter mixed layers. This is likely because the melting of the sea ice releases iron (Boyd & Ellwood, 2010), allows PAR to penetrate into the surface waters, and causes the mixed layer to shoal, all factors that help phytoplankton grow. Prior to the receding of sea ice, the SIZ also experiences polar night and is severely light limited.

Our estimate of phytoplankton seasonality based on profiling floats allows us to critically assess other methods that rely primarily on observations of surface chlorophyll concentrations (Arrigo et al., 2008; Ardyna et al., 2017; Moore & Abbott, 2000; Thomalla et al., 2011). Some recent studies have tried to consider evolution of the bulk biomass, rather than just the surface signature, using ancillary mixed-layer depth estimates and an assumption of vertical homogeneity of phytoplankton concentration over the depth of the mixed layer (Behrenfeld, 2010; Sallée et al., 2015). However, this is no substitute for truly depth-dependent measurements. As was shown in Figures 2e and 2f, our results suggest that in the Southern Ocean, such surface-derived estimate can underestimate the bulk biomass and sometimes even fail to reproduce the temporal variability. We define the surface concentration (C_p^{surf}) as the average concentration in the top 50 dbar, similar to Chl^{surf}. This averaging depth is arbitrary, but changing this depth criterion did not influence the results qualitatively. A corresponding proxy for bulk biomass is then estimated by multiplying C_p^{surf} by the observed mixed-layer depth (h_{ML}), similar to the estimate used by Sallée et al. (2015). The dashed green lines in the bottom row of Figure 2 show that this proxy for bulk biomass has limited success. The proxy bulk biomass captures the approximate seasonal pattern for the float to the south of the sACCF (Figure 2d), as both $\langle C_p \rangle$ and $C_p^{surf} \times h_{ML}$ peak in January. However, $C_p^{surf} \times h_{ML}$ is out of phase with $\langle C_p \rangle$ for the example float in the gyre (Figure 2f), where the mixed layers are shallow, and a significant amount of biomass is present below the mixed-layer base. The comparison for the example float in the ACC is also less than satisfactory (Figure 2e), with the proxy showing weaker amplitude and estimating the apex too soon. Comparing $\langle C_p \rangle$ and $C_p^{surf} \times h_{ML}$ over the whole time series of each float showed that the latter is smaller in amplitude than the former, and the difference is greater at northern latitudes (Figures 2 and S7–S9).

We examined all SOCCOM and SOCLIM float profiles and found this relation ($\langle C_p \rangle > C_p^{surf} \times h_{ML}$) to hold in most cases (Figures 4a and 4b). In particular, the ratio of the maximum of $\langle C_p \rangle$ to $C_p^{surf} \times h_{ML}$, namely, the bulk biomass at the apex defined using each variable, is generally larger than unity (Figure 4b). We also show the timing of the apex defined by the maximum of the proxy, surface biomass (C_p^{surf}), and chlorophyll (Chl^{surf}) concentrations in Figures 3d–3f. The proxy bulk biomass in the northernmost zones tends to reach its apex around September–October, roughly a month earlier compared to Figures 3a–3c in each sector, consistent with Figures 2f and S9. In contrast, if we use C_p^{surf} and Chl^{surf} to detect the apex timing similar to Ardyna et al. (2017), we find that the spread increases, and the median is delayed by a month around December in

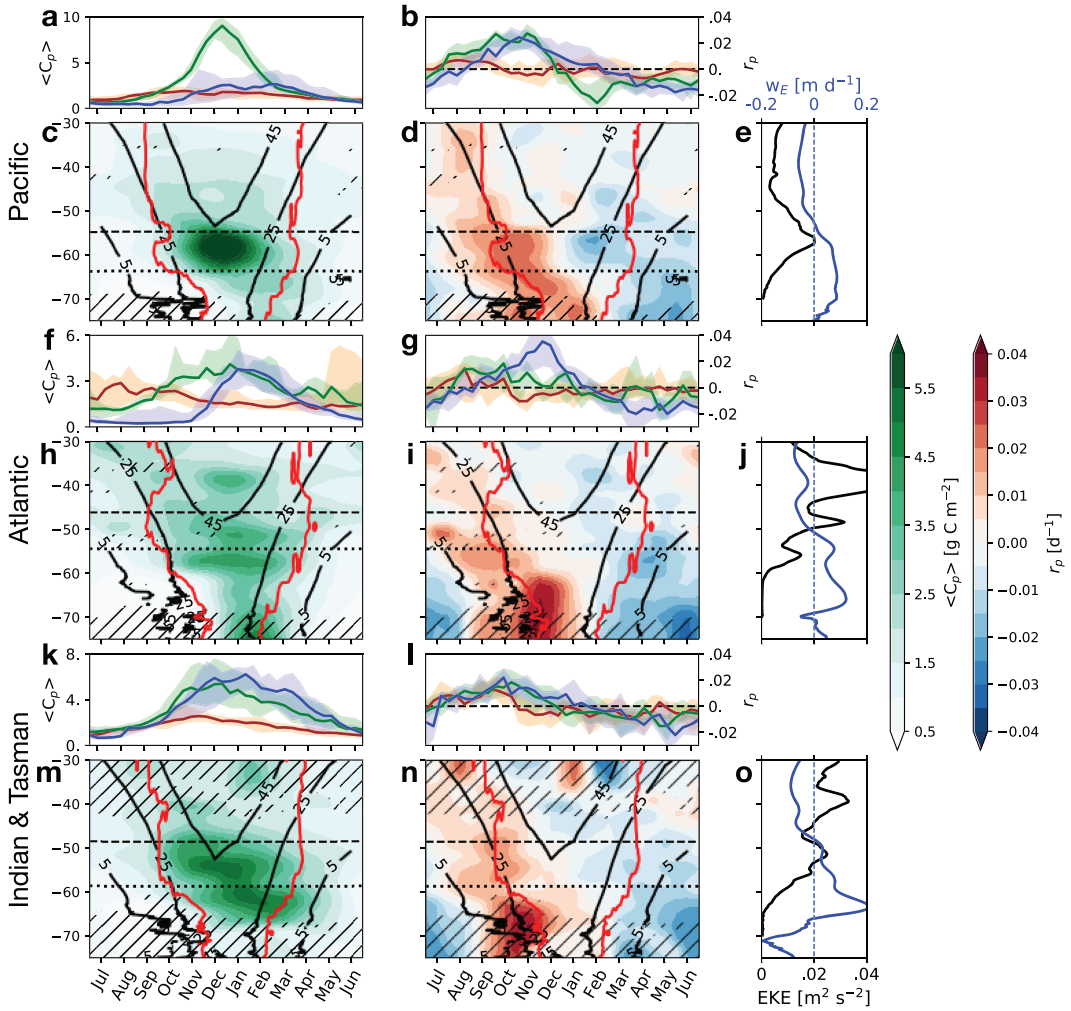

Figure 5. Time series of the 10-day median of $\langle C_p \rangle$ and r_p for each bioregion in the Pacific (a,b), Atlantic (f,g), and InTas (k,l) sectors defined in Table 1. The northernmost zones are shown in orange, southernmost in blue, and middle in green, and the shadings indicate the interquartile range. (c,d,h,i,m,n) Hovmöller diagrams of the monthly and zonally averaged $\langle C_p \rangle$ and r_p plotted against latitude in each sector for the 5 years of float data available. The black hashes indicate grids with less than 10 profiles, the black dashed line shows the zonal mean of the climatological position of the SAF, and the black dotted line shows the climatological sACCF. The black contours show the zonal-mean monthly climatology of surface PAR (5, 25, and 45 Ein·m^{-2}·day^{-1}) observed from the SeaWiFS satellite and the time at which the sign of temperature flux changes taken from the B-SOSE is shown in red contours. (e,j,o) The zonal mean of climatological surface EKE (black) and Ekman pumping (w_E) derived from wind stress in B-SOSE (blue) for each sector.

the northernmost zones (Figures 3e and 3f). However, when we consider zones that are further south, we find better agreement between the apex detected by $\langle C_p \rangle$ and other proxies, likely due to a tighter coupling between the surface and subsurface phytoplankton concentrations (e.g., Figures 2a and S4). Overall, the proxies seem to yield correct estimates of the apex timing south of the SAF but underestimate the bulk biomass across the entire Southern Ocean.

4.3. Zonal and Monthly Mean Characteristics

The previous sections discussed different bloom phases observed by individual floats and the statistics of their timings. In this section we provide a Eulerian view by averaging the bulk phytoplankton biomass and accumulation rates in three zonal sectors: the Pacific, Atlantic, and InTas sectors of the Southern Ocean. The choice to average zonally, while maintaining a distinction between the three sectors, is motivated by the sparse spatial coverage of the data set and the quasi-zonal nature of ACC fronts in each sector. Monthly and zonally averaged Hovmöller diagrams (Figure 5) in latitude versus time were generated by averaging over

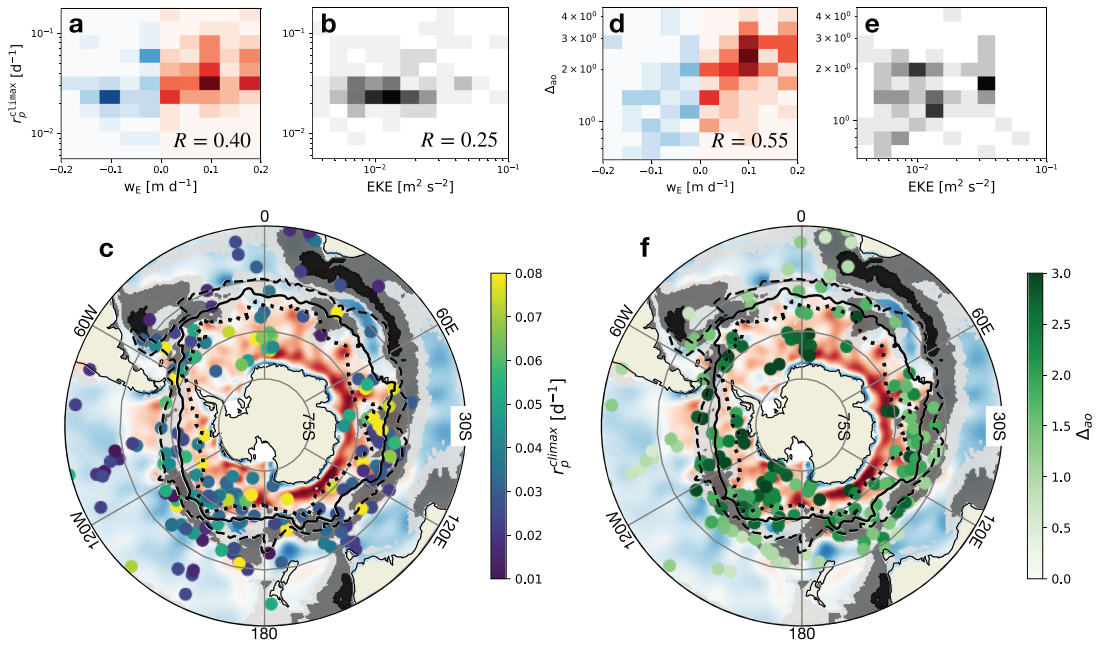

Figure 6. Joint histogram of the accumulation rate at the climax of each bloom (r_p^{climax}) plotted against climatological w_E and surface EKE (a,b). Ekman upwelling (downwelling) is shown in red (blue) and for the histogram with EKE, we take the values north of the sACCF to avoid blooms affected by glaciers and sea ice. (c) Accumulation rates plotted against geographical locations. Red (blue) shadings show the climatological Ekman upwelling (downwelling) taking the wind-stress curl from B-SOSE after a Gaussian spatial filter with 3° radius was applied. The black contours show the climatology of surface EKE in [m^2 s^{-2}] over the years of 1997–2017. Values below 0.009 m^2 s^{-2} are masked out. The SAF, PF, and sACCF are shown in black dashed, solid, and dotted lines, respectively. (d–f) Same for Δ_{ao}. The correlation coefficients (R) are given at 98% confidence level. Δ_{ao} and EKE did not show a statistically significant correlation.

all the data points in a zonal sector after weighting the data points with a Gaussian kernel of width 1.6° in latitude and 0.43 months (Locally Weighted Scatterplot Smoothing). The area of the Gaussian kernel was set to be roughly equivalent to a top-hat kernel with a width of 4° in latitude and 1 month. As $\langle C_p \rangle$ followed roughly a log-normal distribution, we applied the Gaussian kernel to $\ln\langle C_p \rangle$ and then took the exponential of the filtered data.

The climatology of bulk vertically integrated biomass $\langle C_p \rangle$ shows a clear seasonal cycle, with one major bloom per year (Figures 5c, 5h, and 5m). Higher values of $\langle C_p \rangle$(>2 g C m^{-2}) are mostly confined to the months when surface heat flux ($\mathcal{H}$) is positive during the austral summer (zero crossing of mean flux is shown as red lines). Due to shorter summers, indicated by PAR (black contours), blooms are constrained to fewer months in the south, while the northern blooms are more diffused, consistent with the spread in bloom phase timings shown in Figure 3. Since the bioregions have zonal variability (Table 1; Ardyna et al., 2017; Thomalla et al., 2011), we also show the time series of the 10-day median of $\langle C_p \rangle$ for each zone per sector defined in Table 1 (Figures 5a, 5f, and 5k). The Hovmöller diagrams and time series are in sync with each other with the timing of the apex shifting later in the year further south.

In conjunction with biomass, the accumulation rates (r_p) are also evaluated in the same manner (Figures 5b, 5d, 5g, 5i, 5l, and 5n). The zonally averaged accumulation starts ($r_p > 0$) substantially before the timing of the mixed-layer depth maxima (not shown) or when heat flux switches sign and after surface PAR becomes larger than 5 Ein·m^{-2}·day^{-1}. At the time scales under consideration, the lag between change in heat flux and mixed-layer restratification is not discernible (Taylor & Ferrari, 2010, 2011). Phytoplankton accumulation starting during the mixed-layer deepening phase is in agreement with the timing plots in the previous section, where onset happens before the deepest mixed layers are observed. This observation is in agreement with the dilution-recoupling hypothesis of Behrenfeld (2010), which suggests that a deepening mixed layer reduces the phytoplankton and zooplankton concentrations and thus grazing pressure. These reduced grazing rates result in bulk phytoplankton increase, while the concentration of phytoplankton might be very low and even decreasing. The peak accumulation rates are often observed closer to the time when the heat flux changes sign, particularly around 50–60° S, indicating a possible acceleration in growth rates as the

mixed layers start to shoal (similar to those observed in the North Atlantic; Mignot et al., 2018) along with an increase in PAR from winter to spring (Llort et al., 2015).

Figures 5e, 5j, and 5o show the climatological zonal mean of Ekman pumping and surface EKE in each sector plotted against latitude. The seasonal amplitude of $\langle C_p \rangle$ is generally low at latitudes where Ekman pumping is negative ($w_E < 0$) north of the SAF. Local maxima of $\langle C_p \rangle$ align with the zonal-mean EKE maxima associated with the ACC between the SAF and sACCF in each sector, with correspondence in the Pacific being the most prominent (Figure 5). To our knowledge, this sector of the Pacific has the fewest sources of lithogenic/benthic iron among the sectors (Ardyna et al., 2019; Boyd & Ellwood, 2010), so the fact that the Pacific has the largest amplitude in biomass is surprising (Figures 5a and 5c). The correlation between $\langle C_p \rangle$ and EKE with latitude may suggests that vertical eddy transport may be supplying iron along the outcropping isopycnals in the ACC region for the blooms in the Pacific (Freilich & Mahadevan, 2019; Gnanadesikan et al., 2015; Rosso et al., 2014, 2016). The maximum in EKE around 40° S in the Atlantic and InTas sectors comes from a combination of the Brazil, Agulhas, East Australia, and Leewin Current (Figures 6j and 6o). The InTas sector does not display a significant peak in $\langle C_p \rangle$ at corresponding latitudes, but this may be fortuitous due to sparse data coverage particularly in the Indian sector (Figure 1c).

5. Discussion and Conclusions

The seasonal cycle of phytoplankton carbon biomass in the open Southern Ocean has long been of interest to the oceanographic and BGC community, due to its relevance to the biological carbon pump. Satellite observations have greatly enhanced our understanding of this seasonal cycle and the factors controlling its dynamics (e.g., Ardyna et al., 2017; Arrigo et al., 2008; Field et al., 1998; Moore & Abbott, 2000; Sallée et al., 2015; Thomalla et al., 2011; Venables & Moore, 2010). Satellites, however, only capture the surface signature of primary production and can be limited by the presence of clouds and sea ice, which are plentiful in the Southern Ocean. Here, we present the first in situ estimates of phytoplankton carbon biomass seasonality in the open Southern Ocean observed by the BGC Argo floats deployed by the SOCCOM and SOCLIM projects. While limited in spatial coverage relative to satellites, these autonomous platforms provide year-round profiles of optical backscatter in the top 2,000 m, allowing us to provide an estimate independent of chlorophyll, which is known to vary depending on the species and physiological state of phytoplankton (Behrenfeld & Boss, 2003; Cullen, 1982; Erickson & Thompson, 2018; Geider, 1987; Geider et al., 1998; Haëntjens et al., 2017) and to explore the three-dimensional structure of phytoplankton dynamics. Our results suggest that using surface chlorophyll concentrations to detect the apex of the spring bloom can result in timing estimates that are delayed ~1 month compared to when the vertically integrated biomass actually reaches its seasonal maximum and vice versa when using the proxy bulk biomass ($C_p^{surf} \times h_{ML}$) particularly north of the SAF (Figures 3a–3d and 3f). While the comparison made here is not completely fair to satellite-based studies, it does suggest that some caution is needed when interpreting them; regardless of the depth of the mixed layer, satellite observations may miss subsurface vertical structures in BGC variables (Carranza et al., 2018; Lacour et al., 2017). Some promising results have been shown by Behrenfeld et al. (2017) using Light Detection And Ranging sensors, which penetrate the water column deeper than satellite ocean color measurements, and may overcome this shortcoming of remotely sensed observations.

It is interesting to see whether spatial patterns in bloom phenology emerge from our data set. We define two metrics: (i) the rate of increase in biomass at the bloom climax (r_p^{climax}) and (ii) amplitude of the bloom between onset and apex, that is, Δ_{ao} $(= \ln[\langle C_p \rangle]^{apex} - \ln[\langle C_p \rangle]^{onset})$. The former indicates the rate at which biomass increases most rapidly per bloom. The two metrics (r_p^{climax} and Δ_{ao}) are plotted against geographical locations in Figures 6c and 6f. We also show the climatological rates of Ekman pumping calculated from Biogeochemical Southern Ocean State Estimate reanalysis outputs of wind stress ($w_E = \frac{1}{\rho_0 f}\hat{\mathbf{z}}\cdot\nabla\times\tau$) and EKE observed from AVISO sea-surface height (SSH) fields in Figure 6. The Ekman pumping shows the widely known pattern of downwelling ($w_E < 0$; blue) in the subtropical gyres to the north of the ACC and upwelling ($w_E > 0$; red) in the ACC and south of it. The EKE is highest in the ACC, particularly over regions where the ACC interacts with topography (Wilkin & Morrow, 1994).

Both metrics (r_p^{climax} and Δ_{ao}) show a positive correlation with Ekman pumping; larger values coincide with Ekman upwelling ($w_E > 0$) and vice versa (Figures 6a, 6c, 6d, and 6f). The geographical correspondence is consistent with our Hovmöller diagrams (Figure 5) and regions previously shown to have low seasonal

amplitudes of surface chlorophyll (Ardyna et al., 2017; Thomalla et al., 2011). This correspondence in part might result from the mean Ekman upwelling directly bringing nutrients into the productive layers, but this is likely a small contribution due to upwelling rates being extremely slow (Tagliabue et al., 2014). The more dominant way for Ekman forcing to modulate phytoplankton production is by setting the background stratification and ferricline properties (Boyd & Ellwood, 2010) and allowing for tracer transport including iron along isopycnals (Freilich & Mahadevan, 2019; Naveira Garabato et al., 2017). To the north of the SAF, Ekman downwelling results in a deep nutricline and nutrient limitation year round (McClain et al., 2004; Wilson & Coles, 2005), likely causing low values of r_p^{climax} and Δ_{ao}. The very high rates to the south of the sACCF are likely associated with the iron fertilization via glacial and sea ice melt (Ardyna et al., 2019; Boyd & Ellwood, 2010; Boyd et al., 2012; McGillicuddy et al., 2015).

Previous studies have argued that iron limitation is relieved in the open Southern Ocean by the deep winter mixed layers and diapycnal mixing by storms tapping into the ferricline (Llort et al., 2015, 2019; Nicholson et al., 2016; Tagliabue et al., 2014). Elevated rates of production in the ACC, where isopycnals outcrop, might also be suggestive of (sub)mesoscale iron supply at work (Figure 5; Rosso et al., 2014, 2016). Although modest, r_p^{climax} shows a positive correlation with climatological surface EKE in the ACC north of the sACCF (Figures 6b and 6c). It is, however, difficult to exactly disentangle the eddy-driven transport of deep water to the surface from the localized lithogenic and benthic sources of iron in the ACC. The two mechanisms may interact, with the benthic sources releasing iron into deep waters near topography, which are then brought to the surface via strong along-isopycnal and lateral eddy stirring (Ardyna et al., 2017, 2019; d'Ovidio et al., 2015; Freilich & Mahadevan, 2019; Gnanadesikan et al., 2015; Naveira Garabato et al., 2017). Johnson et al. (2017) showed that the ANCP was highest in the ACC region where the mixed layers were the deepest. One might expect light limitation driven by deep mixing to produce the lowest ANCP rates in this region, but it appears that the dissolved iron supplied by high rates of mixing and stirring acts to reduce the chronic iron limitation in the open Southern Ocean (Figure 5).

We also examine whether the existence of regions with high abundance of coccolithophores known as the "Great Calcite Belt" could affect our results. The amplitude Δ_{ao} shows elevated values eastward of the Drake Passage, Weddell Gyre, Prydz Bay, and Ross Sea where we would expect high concentrations of coccolithophores (e.g., Balch et al., 2011, Figure 1 in their paper), but they do not necessarily coincide with high values of r_p^{climax}. Better data coverage would be required, however, to confirm the zonal variations in r_p^{climax} and Δ_{ao} that might be present in each sector.

We have presented the basin-wide averaged annual phytoplankton cycle in the Southern Ocean from in situ observations (Figures 3 and 5) and have only scratched the surface of what can be learned from this growing data set. We hope that this work will spur the interest of the wider community to further explore and critique this data set and perform dedicated investigations into some of the more speculative elements of spatial variability (Figure 6). Regional scale investigations (e.g., Ardyna et al., 2019; Prend et al., 2019) are needed to understand the details of the spatial variations in biogeochemistry. In particular, our interpretation of the annual cycle of phytoplankton has relied on bottom-up processes such as nutrient and surface PAR conditions. However, depth-integrated PAR, rather than surface conditions, is relevant for phytoplankton growth (Boss & Behrenfeld, 2010). Behrenfeld (2010) and Behrenfeld and Boss (2018) also show that the accumulation rates are sensitive to the loss rates due to mortality and grazing. While our data set does not provide direct constraints on the loss rates and depth profile of PAR, efforts should be directed toward making in situ measurements and studying their impact on phytoplankton phenology. Careful investigations are also needed to understand the biases introduced in the observations of time series by the Argo float quasi-Lagrangian sampling and 10-day temporal resolution and the potential for studying synoptic time scale variability. The precise impact and the biases introduced by the float sampling with a coarse temporal resolution (~10 days) could be addressed in the future using an Observing System Simulation Experiment. Our results show that vertically integrated biomass can be high even if concentration itself is low. Depending on the timing of blooms, wintertime enhancement in submesoscale vertical velocities can subduct this organic matter to depth (Erickson & Thompson, 2018; Lacour et al., 2017, 2019; Llort et al., 2018; Omand et al., 2015). Quantifying the timing and biomass of blooms, therefore, can have significant implications for estimating the biological carbon pump.

Acknowledgments
This research was supported by NASA Award NNX16AJ35G as part of the SWOT Science Team. Abernathey acknowledges additional support from NSF Award OCE-1553593. Prend is supported by an NSF Graduate Research Fellowship under Grant DGE-1650112. Gille acknowledges NSF awards PLR-1425989 and OCE-1658001. We thank Joan Llort and another anonymous reviewer for very useful comments on the manuscript. The code used for the analysis in this study is available on Github (doi:10.5281/zenodo.3336575). Data were collected and made freely available by the Southern Ocean Carbon and Climate Observations and Modeling (SOCCOM) Project funded by the National Science Foundation, Division of Polar Programs (NSF PLR -1425989), supplemented by NASA (NNX14AP49G), the Southern Ocean and Climate Field Studies with Innovative Tools (SOCLIM) Project funded by the Foundation BNP Paribas and the Massachusetts Water Resource Authority, and by the International Argo Program and the NOAA programs that contribute to it (http://www.argo.ucsd.edu and http://argo.jcommops.org). The BGC-Argo data used for this study can be downloaded from http://soccom.ucsd.edu/floats/SOCCOM&urluscore;data&urluscore;ref.html for SOCCOM and ftp://ftp.ifremer.fr/ifremer/argo for SOCLIM. Computational resources for B-SOSE were provided by NSF XSEDE resource Grant OCE130007. AVISO products were processed by SSALTO/DUACS and distributed by AVISO+ (https://www.aviso.altimetry.fr) with support from CNES. Photosynthetically available radiation measurements from SeaWiFS were downloaded online (https://oceandata.sci.gsfc.nasa.gov/SeaWiFS/Mapped/Monthly&urluscore;Climatology/9km/par/). The geographical plots were generated using Cartopy (Met Office, 2010-2010-2015).

References

Ardyna, M., Claustre, H., Sallée, J.-B., D'Ovidio, F., Gentili, B., Van Dijken, G., et al. (2017). Delineating environmental control of phytoplankton biomass and phenology in the Southern Ocean. *Geophysical Research Letters*, *44*, 5016–5024. https://doi.org/10.1002/2016GL072428

Ardyna, M., Lacour, L., Sergi, S., dOvidio, F., Sallée, J.-B., Rembauville, M., et al. (2019). Hydrothermal vents trigger massive phytoplankton blooms in the Southern Ocean. *Nature Communications*, *10*, 2451.

Arrigo, K. R., van Dijken, G. L., & Bushinsky, S. (2008). Primary production in the Southern Ocean, 1997–2006. *Journal of Geophysical Research*, *113*, C08004. https://doi.org/10.1029/2007JC004551

Balch, W. M., Drapeau, D. T., Bowler, B. C., Lyczskowski, E., Booth, E. S., & Alley, D. (2011). The contribution of coccolithophores to the optical and inorganic carbon budgets during the Southern Ocean Gas Exchange Experiment: New evidence in support of the Great Calcite Belt hypothesis. *Journal of Geophysical Research*, *116*, C00F06. https://doi.org/10.1029/2011JC006941

Balwada, D., Smith, K. S., & Abernathey, R. (2018). Submesoscale vertical velocities enhance tracer subduction in an idealized Antarctic Circumpolar Current. *Geophysical Research Letters*, *45*, 9790–9802. https://doi.org/10.1029/2018GL079244

Behrenfeld, M. J. (2010). Abandoning Sverdrup's critical depth hypothesis on phytoplankton blooms. *Ecology*, *91*(4), 977–989.

Behrenfeld, M. J., & Boss, E. (2003). The beam attenuation to chlorophyll ratio: An optical index of phytoplankton physiology in the surface ocean? *Deep Sea Research Part I: Oceanographic Research Papers*, *50*(12), 1537–1549.

Behrenfeld, M. J., & Boss, E. S. (2018). Student's tutorial on bloom hypotheses in the context of phytoplankton annual cycles. *Global change biology*, *24*(1), 55–77.

Behrenfeld, M. J., Boss, E., Siegel, D. A., & Shea, D. M. (2005). Carbon-based ocean productivity and phytoplankton physiology from space. *Global Biogeochemical Cycles*, *19*, GB1006. https://doi.org/10.1029/2004GB002299

Behrenfeld, M. J., Hu, Y., O'Malley, R. T., Boss, E. S., Hostetler, C. A., Siegel, D. A., et al. (2017). Annual boom–bust cycles of polar phytoplankton biomass revealed by space-based lidar. *Nature Geoscience*, *10*(2), 118.

Blain, S., Sarthou, G., & Laan, P. (2008). Distribution of dissolved iron during the natural iron-fertilization experiment KEOPS (Kerguelen Plateau, Southern Ocean). *Deep Sea Research Part II: Topical Studies in Oceanography*, *55*(5-7), 594–605.

Boss, E, & Behrenfeld, M (2010). In situ evaluation of the initiation of the North Atlantic phytoplankton bloom. *Geophysical Research Letters*, *37*, L18603. https://doi.org/10.1029/2010GL044174

Bowie, A. R., Van Der Merwe, P., Quéroué, F., Trull, T., Fourquez, M., Planchon, F., et al. (2015). Iron budgets for three distinct biogeochemical sites around the Kerguelen Archipelago (Southern Ocean) during the natural fertilisation study, KEOPS-2. *Biogeosciences*, *12*(14), 4421–4445.

Boyd, P. W., Arrigo, K., Strzepek, R., & Dijken, G. (2012). Mapping phytoplankton iron utilization: Insights into Southern Ocean supply mechanisms. *Journal of Geophysical Research*, *117*, C06009. https://doi.org/10.1029/2011JC007726

Boyd, P. W., & Ellwood, M. J. (2010). The biogeochemical cycle of iron in the ocean. *Nature Geoscience*, *3*(10), 675–682.

Briggs, E. M., Martz, T. R., Talley, L. D., Mazloff, M. R., & Johnson, K. S. (2018). Physical and biological drivers of biogeochemical tracers within the seasonal sea ice zone of the Southern Ocean from profiling floats. *Journal of Geophysical Research: Oceans*, *123*, 746–758. https://doi.org/10.1002/2017JC012846

Bushinsky, S. M., Gray, A. R, Johnson, K. S., & Sarmiento, J. L. (2017). Oxygen in the Southern Ocean from Argo floats: Determination of processes driving air-sea fluxes. *Journal of Geophysical Research: Oceans*, *122*, 8661–8682. https://doi.org/10.1002/2017JC012923

Carranza, M. M., & Gille, S. T. (2015). Southern Ocean wind-driven entrainment enhances satellite chlorophyll-a through the summer. *Journal of Geophysical Research: Oceans*, *120*, 304–323. https://doi.org/10.1002/2014JC010203

Carranza, M. M., Gille, S. T., Franks, P. J., Johnson, K. S., Pinkel, R., & Girton, J. B. (2018). When mixed layers are not mixed. Storm-driven mixing and bio-optical vertical gradients in mixed layers of the Southern Ocean. *Journal of Geophysical Research: Oceans*, *123*, 7264–7289. https://doi.org/10.1029/2018JC014416

Carval, T., Keeley, R., Takatsuki, Y., Yoshida, T., Schmid, C., Goldsmith, R., et al. (2014). Argo User's Manual V3. 2, Argo data management. 119 pp., http://www.argodatamgt.org

Cullen, J. J. (1982). The deep chlorophyll maximum: Comparing vertical profiles of chlorophyll a. *Canadian Journal of Fisheries and Aquatic Sciences*, *39*(5), 791–803.

d'Ovidio, F., Della Penna, A., Trull, T. W., Nencioli, F., Pujol, M-I, Rio, M-H, et al. (2015). The biogeochemical structuring role of horizontal stirring: Lagrangian perspectives on iron delivery downstream of the Kerguelen Plateau. *Biogeosciences*, *12*(19), 5567–5581.

de Boyer Montégut, C., Madec, G., Fischer, A. S., Lazar, A., & Iudicone, D. (2004). Mixed layer depth over the global ocean: An examination of profile data and a profile-based climatology. *Journal of Geophysical Research*, *109*, C12003. https://doi.org/10.1029/2004JC002378

Deppeler, S. L., & Davidson, A. T. (2017). Southern Ocean phytoplankton in a changing climate. *Frontiers in Marine Science*, *4*, 40.

Dutkiewicz, S., Follows, M. J., & Parekh, P. (2005). Interactions of the iron and phosphorus cycles: A three-dimensional model study. *Global Biogeochemical Cycles*, *19*, GB1021. https://doi.org/10.1029/2004GB002342

Erickson, Z. K., & Thompson, A. (2018). The seasonality of physically-driven export at submesoscales in the northeast Atlantic Ocean. *Global Biogeochemical Cycles*, *32*, 1144–1162. https://doi.org/10.1029/2018GB005927

Field, C. B., Behrenfeld, M. J., Randerson, J. T., & Falkowski, P. (1998). Primary production of the biosphere: Integrating terrestrial and oceanic components. *Science*, *281*(5374), 237–240.

Forward, R. B. (1976). Light and diurnal vertical migration: Photobehavior and photophysiology of plankton, *Photochemical and photobiological reviews* (pp. 157–209) Durham, North Carolina: Springer.

Fox-Kemper, B., Ferrari, R., & Hallberg, R. (2008). Parameterization of mixed layer eddies. Part I: Theory and diagnosis. *Journal of Physical Oceanography*, *38*(6), 1145–1165.

Freilich, M. A., & Mahadevan, A. (2019). Decomposition of vertical velocity for nutrient transport in the upper ocean. *Journal of Physical Oceanography*, *49*(6), 1561–1575.

Geider, R. J. (1987). Light and temperature dependence of the carbon to chlorophyll a ratio in microalgae and cyanobacteria: Implications for physiology and growth of phytoplankton. *New Phytologist*, *106*(1), 1–34.

Geider, R. J., Maclntyre, H. L., & Kana, T. M. (1998). A dynamic regulatory model of phytoplanktonic acclimation to light, nutrients, and temperature. *Limnology and oceanography*, *43*(4), 679–694.

Gent, P. R., & McWilliams, J. C. (1990). Isopycnal mixing in ocean circulation models. *Journal of Physical Oceanography*, *20*(1), 150–155.

Gille, S. T., Carranza, M. M., Cambra, R, & Morrow, R (2014). Wind-induced upwelling in the Kerguelen Plateau region. *Biogeosciences*, *11*, 6389–6400.

Gnanadesikan, A., Pradal, M.-A., & Abernathey, R. (2015). Isopycnal mixing by mesoscale eddies significantly impacts oceanic anthropogenic carbon uptake. *Geophysical Research Letters*, *42*, 4249–4255. https://doi.org/10.1002/2015GL064100

Graff, J. R., Westberry, T. K., Milligan, A. J., Brown, M. B., Dall'Olmo, G., van Dongen-Vogels, V., et al. (2015). Analytical phytoplankton carbon measurements spanning diverse ecosystems. *Deep Sea Research Part I: Oceanographic Research Papers*, *102*, 16–25.

Gray, A. R., Johnson, K. S., Bushinsky, S. M., Riser, S. C., Russell, J. L., Talley, L. D., et al. (2018). Autonomous biogeochemical floats detect significant carbon dioxide outgassing in the high-latitude Southern Ocean. *Geophysical Research Letters*, *45*, 9049–9057. https://doi.org/10.1029/2018GL078013

Gruber, N., Landschützer, P., & Lovenduski, N. S. (2019). The variable Southern Ocean carbon sink. *Annual review of marine science*, *11*, 159–186.

Haëntjens, N., Boss, E., & Talley, L. D. (2017). Revisiting ocean color algorithms for chlorophyll a and particulate organic carbon in the Southern Ocean using biogeochemical floats. *Journal of Geophysical Research: Oceans*, *122*, 6583–6593. https://doi.org/10.1002/2017JC012844

Hauck, J., Völker, C., Wolf-Gladrow, D. A., Laufkötter, C., Vogt, M., Aumont, O., et al. (2015). On the Southern Ocean CO_2 uptake and the role of the biological carbon pump in the 21st century. *Global Biogeochemical Cycles*, *29*, 1451–1470. https://doi.org/10.1002/2015GB005140

Henson, S., Le Moigne, F., & Giering, S. (2019). Drivers of carbon export efficiency in the global ocean. *Global Biogeochemical Cycles*, *33*, 891–903. https://doi.org/10.1029/2018GB006158

Johnson, K. S., Plant, J. N., Coletti, L. J., Jannasch, H. W., Sakamoto, C. M., Riser, S. C., et al. (2017). Biogeochemical sensor performance in the SOCCOM profiling float array. *Journal of Geophysical Research: Oceans*, *122*, 6416–6436. https://doi.org/10.1002/2017JC012838

Lacour, L, Ardyna, M, Stec, K., Claustre, H, Prieur, L, Poteau, A, et al. (2017). Unexpected winter phytoplankton blooms in the North Atlantic subpolar gyre. *Nature Geoscience*, *10*(11), 836.

Lacour, L, Briggs, N, Claustre, H, Ardyna, M, & Dall'Olmo, G (2019). The intraseasonal dynamics of the mixed layer pump in the subpolar North Atlantic Ocean: A biogeochemical-Argo float approach. *Global Biogeochemical Cycles*, *33*, 266–281. https://doi.org/10.1029/2018GB005997

Laufkötter, C., Vogt, M., Gruber, N., Aumont, O., Bopp, L., Doney, S. C., et al. (2015). Projected decreases in future marine export production: The role of carbon fluxes through the upper ocean ecosystem. *Biogeosciences Discussions*, *12*, 19,941–19,998.

Lévy, M., Bopp, L., Karleskind, P., Resplandy, L., Éthé, C., & Pinsard, F. (2013). Physical pathways for carbon transfers between the surface mixed layer and the ocean interior. *Global Biogeochemical Cycles*, *27*, 1001–1012. https://doi.org/10.1002/gbc.20092

Leymarie, E., Penkerc'h, C., Vellucci, V., Lerebourg, C., Antoine, D., Boss, E., et al. (2018). Proval: A new autonomous profiling float for high quality radiometric measurements. *Frontiers in Marine Science*, *5*, 437.

Llort, J., Langlais, C., Matear, R., Moreau, S., Lenton, A., & Strutton, P. G. (2018). Evaluating Southern Ocean carbon eddy-pump from biogeochemical-Argo floats. *Journal of Geophysical Research: Oceans*, *123*, 971–984. https://doi.org/10.1002/2017JC012861

Llort, J., Lévy, M., Sallée, J.-B., & Tagliabue, A. (2015). Onset, intensification, and decline of phytoplankton blooms in the Southern Ocean. *ICES Journal of Marine Science: Journal du Conseil*, *72*(6), 1971–1984.

Llort, J, Lévy, M., Sallée, J.-B., & Tagliabue, A (2019). Nonmonotonic response of primary production and export to changes in mixed-layer depth in the Southern Ocean. *Geophysical Research Letters*, *46*, 3368–3377. https://doi.org/10.1029/2018GL081788

Marshall, J., & Speer, K. (2012). Closure of the meridional overturning circulation through Southern Ocean upwelling. *Nature Geoscience*, *5*(3), 171.

Martin, J. H., Gordon, RM., & Fitzwater, S. E. (1990). Iron in Antarctic waters. *Nature*, *345*(6271), 156.

Mazloff, M. R., Cornuelle, B. D., Gille, S. T., & Verdy, A (2018). Correlation lengths for estimating the large-scale carbon and heat content of the Southern Ocean. *Journal of Geophysical Research: Oceans*, *123*, 883–901. https://doi.org/10.1002/2017JC013408

McClain, C. R., Signorini, S. R., & Christian, J. R. (2004). Subtropical gyre variability observed by ocean-color satellites. *Deep Sea Research Part II: Topical Studies in Oceanography*, *51*(1–3), 281–301.

McDougall, T. J., & Barker, P. M. (2011). Getting started with TEOS-10 and the Gibbs Seawater (GSW) oceanographic toolbox. *SCOR/IAPSO WG*, *127*, 1–28.

McGillicuddy, D. J., Sedwick, P. N., Dinniman, M. S., Arrigo, K. R., Bibby, T. S., Greenan, B. J., et al. (2015). Iron supply and demand in an Antarctic shelf ecosystem. *Geophysical Research Letters*, *42*, 8088–8097. https://doi.org/10.1002/2015GL065727

McKinley, G. A., Fay, A. R., Lovenduski, N. S., & Pilcher, D. J. (2017). Natural variability and anthropogenic trends in the ocean carbon sink. *Annual Review of Marine Science*, *9*(1), 125–150.

Met Office (2010-2015). Cartopy: A cartographic python library with a Matplotlib interface, Exeter, Devon. http://scitools.org.uk/cartopy

Mignot, A., Ferrari, R., & Claustre, H. (2018). Floats with bio-optical sensors reveal what processes trigger the North Atlantic bloom. *Nature Communications*, *9*(1), 190.

Mignot, A., Ferrari, R., & Mork, K. A. (2016). Spring bloom onset in the Nordic Seas. *Biogeosciences*, *13*(11), 3485–3502.

Moore, J., & Abbott, M. (2000). Phytoplankton chlorophyll distributions and primary production in the Southern Ocean. *Journal of Geophysical Research*, *105*(C12), 28,709–28,722.

Moore, J. K., Lindsay, K., Doney, S. C., Long, M. C., & Misumi, K. (2013). Marine ecosystem dynamics and biogeochemical cycling in the Community Earth System Model [CESM1 (BGC)]: Comparison of the 1990s with the 2090s under the RCP4.5 and RCP8.5 scenarios. *Journal of Climate*, *26*(23), 9291–9312.

Moore, C. M., Mills, M. M., Arrigo, K. R., Berman-Frank, I., Bopp, L., Boyd, P. W., et al. (2013). Processes and patterns of oceanic nutrient limitation. *Nature geoscience*, *6*(9), 701.

Morel, A., Huot, Y., Gentili, B., Werdell, P. J., Hooker, S. B., & Franz, B. A. (2007). Examining the consistency of products derived from various ocean color sensors in open ocean (case 1) waters in the perspective of a multi-sensor approach. *Remote Sensing of Environment*, *111*(1), 69–88.

Naveira Garabato, A. C., MacGilchrist, G. A., Brown, P. J., Evans, DGwyn, Meijers, A. J., & Zika, J. D. (2017). High-latitude ocean ventilation and its role in Earth's climate transitions. *Philosophical Transactions of the Royal Society A: Mathematical, Physical and Engineering Sciences*, *375*(2102), 20160324.

Nicholson, S.-A., Lévy, M., Llort, J., Swart, S., & Monteiro, P. (2016). Investigation into the impact of storms on sustaining summer primary productivity in the sub-Antarctic Ocean. *Geophysical Research Letters*, *43*, 9192–9199. https://doi.org/10.1002/2016GL069973

Omand, M. M., D'Asaro, E. A., Lee, C. M., Perry, M. J., Briggs, N., Cetinić, I., & Mahadevan, A. (2015). Eddy-driven subduction exports particulate organic carbon from the spring bloom. *Science*, *348*(6231), 222–225.

Parekh, P., Follows, M. J., & Boyle, E. (2004). Modeling the global ocean iron cycle. *Global Biogeochemical Cycles*, *18*, GB1002. https://doi.org/10.1029/2003GB002061

Prend, C. J., Gille, S. T., Talley, L. D., Mitchell, B. G., Rosso, I., & Mazloff, M. R. (2019). Physical drivers of phytoplankton bloom initiation in the Southern Ocean's Scotia Sea. *Journal of Geophysical Research: Oceans*, 5811–5826. https://doi.org/10.1029/2019JC015162

Redi, M. H. (1982). Oceanic isopycnal mixing by coordinate rotation. *Journal of Physical Oceanography*, *12*(10), 1154–1158.

Rembauville, M., Briggs, N., Ardyna, M., Uitz, J., Catala, P., Penkerc'h, C., et al. (2017). Plankton assemblage estimated with BGC-Argo floats in the Southern Ocean: Implications for seasonal successions and particle export. *Journal of Geophysical Research: Oceans*, *122*, 8278–8292. https://doi.org/10.1002/2017JC013067

Riser, S. C., Swift, D., & Drucker, R. (2018). Profiling floats in SOCCOM: Technical capabilities for studying the Southern Ocean. *Journal of Geophysical Research: Oceans*, *123*, 4055–4073. https://doi.org/10.1002/2017JC013419

Roesler, C., Uitz, J., Claustre, H., Boss, E., Xing, X., Organelli, E., et al. (2017). Recommendations for obtaining unbiased chlorophyll estimates from in situ chlorophyll fluorometers: A global analysis of WET labs ECO sensors. *Limnology and Oceanography: Methods*, *15*(6), 572–585.

Rosso, I., Hogg, A. M., Matear, R., & Strutton, P. G. (2016). Quantifying the influence of sub-mesoscale dynamics on the supply of iron to Southern Ocean phytoplankton blooms. *Deep Sea Research Part I: Oceanographic Research Papers*, *115*, 199–209.

Rosso, I., Hogg, A. M., Strutton, P. G., Kiss, A. E., Matear, R., Klocker, A., & van Sebille, E. (2014). Vertical transport in the ocean due to sub-mesoscale structures: Impacts in the Kerguelen Region. *Ocean Modelling*, *80*, 10–23.

Sallée, J.-B., Llort, J., Tagliabue, A., & Lévy, M. (2015). Characterization of distinct bloom phenology regimes in the Southern Ocean. *ICES Journal of Marine Science: Journal du Conseil*, *72*(6), 1985–1998.

Sarmiento, J. L. (2013). *Ocean biogeochemical dynamics*. Princeton, New Jersey: Princeton University Press.

Schallenberg, C., Bestley, S., Klocker, A., Trull, T. W., Davies, D. M., Gault-Ringold, M., et al. (2018). Sustained upwelling of subsurface iron supplies seasonally persistent phytoplankton blooms around the southern Kerguelen Plateau, Southern Ocean. *Journal of Geophysical Research: Oceans*, *123*, 5986–6003. https://doi.org/10.1029/2018JC013932

Schlitzer, R. (2002). Carbon export fluxes in the southern ocean: Results from inverse modeling and comparison with satellite-based estimates. *Deep Sea Research Part II: Topical Studies in Oceanography*, *49*(9-10), 1623–1644.

Siegel, D. A., Buesseler, K. O., Doney, S. C., Sailley, S. F., Behrenfeld, M. J., & Boyd, P. W. (2014). Global assessment of ocean carbon export by combining satellite observations and food-web models. *Global Biogeochemical Cycles*, *28*, 181–196. https://doi.org/10.1002/2013GB004743

Siegenthaler, U, & Sarmiento, J. (1993). Atmospheric carbon dioxide and the ocean. *Nature*, *365*(6442), 119.

Silsbe, G. M., Behrenfeld, M. J., Halsey, K. H., Milligan, A. J., & Westberry, T. K. (2016). The CAFE model: A net production model for global ocean phytoplankton. *Global Biogeochemical Cycles*, *30*, 1756–1777. https://doi.org/10.1002/2016GB005521

Stukel, M. R., & Ducklow, H. W. (2017). Stirring up the biological pump: Vertical mixing and carbon export in the Southern Ocean. *Global Biogeochemical Cycles*, *31*, 1420–1434. https://doi.org/10.1002/2017GB005652

Swart, S., Speich, S., Ansorge, I. J., & Lutjeharms, J. R. E. (2010). An altimetry-based gravest empirical mode south of Africa: 1. Development and validation. *Journal of Geophysical Research*, *115*, C03002. https://doi.org/10.1029/2009JC005299

Swart, S, Thomalla, S. J., & Monteiro, P. M. S. (2015). The seasonal cycle of mixed layer dynamics and phytoplankton biomass in the Sub-Antarctic Zone: A high-resolution glider experiment. *Journal of Marine Systems*, *147*, 103–115.

Tagliabue, A., Sallée, J.-B., Bowie, A. R., Lévy, M., Swart, S., & Boyd, P. W. (2014). Surface-water iron supplies in the Southern Ocean sustained by deep winter mixing. *Nature Geoscience*, *7*(4), 314–320.

Taylor, J. R., & Ferrari, R. (2010). Buoyancy and wind-driven convection at mixed layer density fronts. *Journal of Physical Oceanography*, *40*(6), 1222–1242.

Taylor, J. R., & Ferrari, R. (2011). Shutdown of turbulent convection as a new criterion for the onset of spring phytoplankton blooms. *Limnology and Oceanography*, *56*(6), 2293–2307.

Thomalla, S. J., Fauchereau, N., Swart, S., & Monteiro, P. M. S. (2011). Regional scale characteristics of the seasonal cycle of chlorophyll in the Southern Ocean. *Biogeosciences*, *8*(10), 2849–2866.

Venables, H., & Moore, C. M. (2010). Phytoplankton and light limitation in the Southern Ocean: Learning from high-nutrient, high-chlorophyll areas. *Journal of Geophysical Research*, *115*, C02015. https://doi.org/10.1029/2009JC005361

Verdy, A., & Mazloff, M. R. (2017). A data assimilating model for estimating Southern Ocean biogeochemistry. *Journal of Geophysical Research: Oceans*, *122*, 6968–6988. https://doi.org/10.1002/2016JC012650

Wilkin, J. L., & Morrow, R. A. (1994). Eddy kinetic energy and momentum flux in the Southern Ocean: Comparison of a global eddy-resolving model with altimeter, drifter, and current-meter data. *Journal of Geophysical Research*, *99*(C4), 7903–7916.

Williams, R. G., & Follows, M. J. (2011). *Ocean dynamics and the carbon cycle: Principles and mechanisms*. Cambridge: Cambridge University Press.

Wilson, C., & Coles, V. J. (2005). Global climatological relationships between satellite biological and physical observations and upper ocean properties. *Journal of Geophysical Research*, *110*, C10001. https://doi.org/10.1029/2004JC002724